Icarus 255 (2015) 58–69

Contents lists available at ScienceDirect

Icarus

journal homepage: www.elsevier.com/locate/icarus

Evidence for exposed water ice in the Moon's south polar regions from Lunar Reconnaissance Orbiter ultraviolet albedo and temperature measurements

Paul O. Hayne [a,*], Amanda Hendrix [b], Elliot Sefton-Nash [c], Matthew A. Siegler [a], Paul G. Lucey [d], Kurt D. Retherford [e], Jean-Pierre Williams [c], Benjamin T. Greenhagen [a], David A. Paige [c]

[a] Jet Propulsion Laboratory, California Institute of Technology, Pasadena, CA 91109, United States
[b] Planetary Science Institute, Pasadena, CA 91106, United States
[c] University of California, Los Angeles, CA 90095, United States
[d] University of Hawaii, Manoa, HI 96822, United States
[e] Southwest Research Institute, Boulder, CO 80302, United States

ARTICLE INFO

Article history:
Received 25 July 2014
Revised 26 March 2015
Accepted 30 March 2015
Available online 3 April 2015

Keywords:
Moon
Ices
Ices, UV spectroscopy
Moon, surface

ABSTRACT

We utilize surface temperature measurements and ultraviolet albedo spectra from the Lunar Reconnaissance Orbiter to test the hypothesis that exposed water frost exists within the Moon's shadowed polar craters, and that temperature controls its concentration and spatial distribution. For locations with annual maximum temperatures T_{max} greater than the H_2O sublimation temperature of ~110 K, we find no evidence for exposed water frost, based on the LAMP UV spectra. However, we observe a strong change in spectral behavior at locations perennially below ~110 K, consistent with cold-trapped ice on the surface. In addition to the temperature association, spectral evidence for water frost comes from the following spectral features: (a) decreasing Lyman-α albedo, (b) decreasing "on-band" (129.57–155.57 nm) albedo, and (c) increasing "off-band" (155.57–189.57 nm) albedo. All of these features are consistent with the UV spectrum of water ice, and are expected for water ice layers >~100 nm in thickness. High regolith porosity, which would darken the surface at all wavelengths, cannot alone explain the observed spectral changes at low temperatures. Given the observed LAMP off-band/on-band albedo ratios at a spatial scale of 250 m, the range of water ice concentrations within the cold traps with T_{max} < 110 K is ~0.1–2.0% by mass, if the ice is intimately mixed with dry regolith. If pure water ice is exposed instead, then up to ~10% of the surface area on the 250-m scale of the measurements may be ice-covered. The observed distribution of exposed water ice is highly heterogeneous, with some cold traps <110 K having little to no apparent water frost, and others with a significant amount of water frost. As noted by Gladstone et al. (Gladstone, G.R. et al. [2012]. J. Geophys. Res.: Planets 117(E12)), this heterogeneity may be a consequence of the fact that the net supply rate of H_2O molecules to the lunar poles is very similar to the net destruction rate within the cold traps. However, an observed increase in apparent H_2O abundance with decreasing temperature from ~110 K to 65 K suggests that destruction of surface frosts by impact gardening and space weathering is spatially heterogeneous. We find a loosely bimodal distribution of apparent ice concentrations with temperature, possibly due to competition between vertical mixing by impact gardening and resupply of H_2O by vapor diffusion at sites ~110 K. Finally, we cannot rule out the possibility that the colder population of ice deposits is in fact primarily carbon dioxide ice, although peak temperatures of ~65 K are slightly higher than the usual CO_2 sublimation temperature of ~60 K.

© 2015 Elsevier Inc. All rights reserved.

1. Introduction

Water ice and other volatiles may be present within cold traps near the lunar poles, where temperatures are low enough to prevent significant sublimation losses over billion-year time scales (Watson et al., 1961). Remote sensing by orbital spacecraft, and

* Corresponding author at: Jet Propulsion Laboratory, California Institute of Technology, MS 183-301, 4800 Oak Grove Drive, Pasadena, CA 91109, United States.
E-mail address: Paul.O.Hayne@jpl.nasa.gov (P.O. Hayne).

http://dx.doi.org/10.1016/j.icarus.2015.03.032
0019-1035/© 2015 Elsevier Inc. All rights reserved.

the Lunar Crater Observation and Sensing Spacecraft (LCROSS) impact experiment provide compelling evidence for the existence of cold-trapped volatiles, but their abundance, composition, and distribution remain uncertain (e.g., Nozette et al., 1996; Feldman et al., 1998; Colaprete et al., 2010; Gladstone et al., 2010a). Improved constraints on lunar volatile composition could help identify possible origins, including comet and asteroid impacts, solar wind ion implantation, and outgassing of primordial volatiles from the lunar interior. Although temperatures are perennially below the ~110-K threshold to cold-trap water ice (and many other volatile compounds) over vast regions near the lunar poles (Paige et al., 2010a), the rates of supply, burial, excavation, and destruction are not known (Arnold, 1979). Several ground-based searches for ice in polar craters using radar backscatter turned up no evidence for macroscopic ice (blocks >~10 cm) within ~1 m of the surface (Stacy et al., 1997; Campbell et al., 2006). This result is in stark contrast to similar radar investigations of the planet Mercury, where extensive polar ice deposits were discovered (Slade et al., 1992). However, the LCROSS impact, which excavated down to ~2–3 m depth at one of the coldest places on the Moon (Schultz et al., 2010; Hayne et al., 2010), exhumed material containing ~5–7 wt% water ice and smaller amounts of other volatiles likely originating in comets (Colaprete et al., 2010). This ice could occur as small-grained water frost at the surface, intimately mixed ice and regolith grains, or subsurface ice layers.

Recent results from two instruments on the Lunar Reconnaissance Orbiter (LRO) spacecraft suggest the presence of water frost at the Moon's surface: (1) the Lunar Orbiter Laser Altimeter (LOLA) measured anomalously high albedo at 1064 nm wavelength within Shackleton crater at the lunar south pole (Zuber et al., 2012), and (2) the Lyman Alpha Mapping Project (LAMP) measured lunar ultraviolet (UV) albedo spectra exhibiting an absorption at wavelengths ~100–160 nm (Gladstone et al., 2012; Hendrix et al., 2012; Lucey et al., 2014). Also, data from the Lunar Prospector Neutron Spectrometer (LP-NS) appear consistent with the interpretation of the high LOLA albedo at Shackleton crater being due to surface water frost (Miller et al., 2014). Nonetheless, it is unclear whether these putative surface frosts occur in places where they would be most thermally stable. For example, although much of Shackleton crater remains perennially below 110 K, there are many other, colder craters that apparently lack a similar 1064-nm albedo enhancement. In fact, data from the Kaguya spacecraft suggest that Shackleton's albedo enhancement may be due to its feldspathic composition, rather than water frost (Haruyama et al., 2008, 2013). Radar de-polarization data for Shackleton (and other polar craters) are most consistent with roughness effects, although up to ~5–10 wt% ice cannot be ruled out (Thomson et al., 2012). Craters showing UV spectra consistent with enhanced surface water frost do not immediately appear correlated with the coldest temperatures (cf. Gladstone et al., 2012; Paige et al., 2010a), although no systematic study of the Moon's temperature-UV albedo correlation has been done to date.

We investigated the relationships between lunar surface and subsurface temperatures and UV albedo spectra, using data from LRO's Diviner (Paige et al., 2010b) and LAMP (Gladstone et al., 2010b) instruments. Temperature data from Diviner, along with thermal models, constrain the locations where water ice would be thermodynamically stable, whereas the LAMP albedo data constrain the presence and abundance of water frost at the optical surface (~1–10 wavelengths, or ~0.1–1 μm). Diviner data present an opportunity to test the hypothesis that temperature controls the distribution of water frost in the Moon's polar regions. If water frost is present at the surface, this could represent a valuable resource for future *in situ* extraction and scientific analysis or resource utilization. Therefore, improved knowledge of the distribution of surface frost on the Moon would enable future missions to study and utilize lunar volatiles.

2. Data

Both the Diviner and LAMP datasets used here have sufficiently high signal-to-noise ratios (SNR) in the lunar south polar region (pole-ward of 80°S). LAMP uses starlight and emissions from interplanetary hydrogen as illumination sources to measure the UV reflectance of the lunar night side and permanently shadowed regions. Due to the prevalence of UV-bright stars in the Moon's southern hemisphere, LAMP acquires data with much better SNR near the south pole, whereas we found that the available north polar data were not adequate for this study. Fortunately, as LAMP continues to acquire data, the SNR will continue to increase, which may allow for future studies of the lunar northern polar region.

2.1. Diviner

Diviner is a nine-channel filter radiometer, with two solar and seven infrared spectral channels spanning wavelengths from ~0.3 to >100 μm (Paige et al., 2010b). We calculate and map bolometric brightness temperature, the wavelength-integrated radiance in all seven of Diviner's thermal channels expressed as the temperature of an equivalent blackbody (Paige et al., 2010a). Assuming thermal equilibrium, bolometric brightness temperature (T_{bol}) is the best representation of surface kinetic temperature based on thermal emission. Diviner data used in this analysis were acquired between July 5th 2009 and November 1st 2013 and in the latitude range 82.5–90°S.

The effective field of view (EFOV) for each Diviner observation describes the likelihood of photons being incident on the detector within an observation's time-integrated footprint. The EFOV is defined by three functions: (i) the in-track smear due to spacecraft motion relative to the Moon, $b(t)$, (ii) the detector response as a function of time, $d(t)$, and (iii) the instantaneous field of view $\phi(t)$. These functions are defined through knowledge of observation geometry and instrument specifications detailed in Paige et al. (2010b). For each observation, we construct a 2D probability distribution in the focal plane of the detector – equal to a convolution of the component functions evaluated over the integration time: $[(b * d) * \phi](t)$. To produce gridded map products from many observations, each EFOV is then modeled as a Monte Carlo distribution of 100 points, each representing 1/100th of the original observation (Sefton-Nash et al., 2014).

Mapped EFOVs from successive orbits increasingly overlap towards the poles, often with many repeat observations of the same location. Simply binning all available data from each channel onto a grid then calculating bolometric temperature would be incorrect because observations from different orbits are acquired at least 113 min apart and therefore potentially under different solar illumination conditions and/or thermal states (for shadowed regions). For example, one pixel could include data from two places both falling within overlapping, but different, EFOVs. The two places may never both be illuminated at the same time, but would both contribute to the same bolometric brightness temperature calculation, artificially inflating the apparent temperature.

To avoid such errors, we first calculate bolometric brightness temperature within each orbit track only, where observations with overlapping EFOVs are on the order of seconds, rather than hours apart. Data from each orbit and channel are then binned onto a south polar stereographic grid of resolution 76.4 m pixel^{-1} (at the latitude of true scale, 90°S). Bolometric brightness temperature

grids for each orbit are then compounded to produce maximum, minimum and average bolometric brightness temperature maps.

2.2. LAMP

LAMP measures ultraviolet radiation reflected from the lunar surface, where the illumination source is starlight and emissions from hydrogen in the interplanetary medium. We used publicly available gridded polar LAMP data products from NASA's Planetary Data System (PDS), dated 6 March, 2011. These gridded data records (GDR) consist of average albedo and statistical uncertainties in 250 m-per-pixel bins, within four spectral bands: Lyman-α (119.57–125.57 nm), "long" (129.57–189.57 nm), "on-band" (129.57–155.57 nm), and "off band" (155.57–189.57 nm). The off-band and on-band wavelengths refer to the position of a strong water absorption feature, such that water frost has near-zero albedo in the on-band region (<160 nm), and albedo near-unity in the off-band region (Hendrix et al., 2010). Therefore, the off-band/on-band ratio is expected to be high where any water frost is present on the surface (Gladstone et al., 2012). For this work, we downloaded the on- and off-band GDR separately and generated the ratio manually, which resulted in a less noisy ratio map than the one available on the PDS. We propagated the statistical uncertainties from the individual points in the on- and off-band maps in order to derive the errors for the ratio map.

To improve the quality of the dataset, we first rejected individual spatial bins with signal-to-noise ratios <1. Then, we applied a 9×9 pixel (5 km^2) spatial median filter, in order to eliminate outliers. We found this procedure significantly reduced the statistical uncertainties, and brought out the major features in the LAMP maps. Fig. 1 shows an example of the "before" and "after" products for the off-band data.

3. Albedo model

To simulate the reflectance spectra of lunar regolith and surface frost, we used the two-stream delta-Eddington method developed by Wiscombe and Warren (1980). The model calculates directional-hemispheric albedo, which is the ratio of the total power reflected into the full hemisphere to the power in the (collimated) incident beam. By the principle of reciprocity, this is identical to the albedo measured by LAMP, if the incident UV radiation is diffuse and assuming the instrument field of view is narrow. We used water ice optical constants from Warren and Brandt (2008), and a modified version of the lunar regolith simulated optical constants as in Hendrix et al. (2012). For the latter, we found it necessary to adjust the imaginary component of the refractive index using the scaling $k' = (k + 2)/2.5$, in order to match the LAMP albedo for non-cold trap regions.

Although other volatiles may be present within the cold traps, they are likely to be less abundant than water frost (Watson et al., 1961; Colaprete et al., 2010). We therefore limited the spectral modeling to water frost and lunar regolith. The optical effective particle size for lunar regolith (r_{eff} = 32 μm, Hayne et al., 2010) and water ice (r_{eff} = 5.0 μm, similar to the regolith pore size) are both much larger than the wavelength (i.e. size parameter >100), such that scattering properties can be approximated by geometric optics. Nonetheless, Mie theory provides a robust calculation of optical properties for a range of size parameter and composition, including mixtures. We used the standard Mie code developed and maintained by the University of Oxford (http://eodg.atm.ox.ac.uk/). Following Hapke (1993), the Mie scattering parameters f_{mix} for intimate mixtures of N components f_i are calculated by

$$f_{mix} = \sum_{i=1}^{N} Q_i r_i^2 n_i f_i \Big/ \sum_{i=1}^{N} Q_i r_i^2 n_i, \quad (1)$$

where Q_i is the extinction efficiency, r_i the particle radius, and n_i the number density of the ith component. Using Eq. (1), we calculate Mie parameters for mixtures of water ice and regolith, which are then used to model the albedo spectra for each given ice concentration.

Fig. 2 shows model spectra for pure water ice and the lunar regolith model. A "red" ultraviolet spectral slope is consistent with measured LAMP spectra of both highlands and maria units (Hendrix et al., 2012), whereas water ice exhibits a strongly blue slope near 160 nm wavelength, between the off-band and on-band wavelengths. In the Ly-α and on-band spectral regions, water ice is nearly black (i.e. zero albedo). In the off-band region, water ice is nearly a perfect reflector. Heterogeneous distributions of ice and regolith within the LAMP field of view would result in a spectrum linearly proportional to their relative surface areas. Fig. 2 also shows the modeled UV spectral appearance of intimate mixtures of regolith and water ice, from zero to 5% (by mass) of water ice in increments of 0.1%. Off-band albedo rapidly increases with

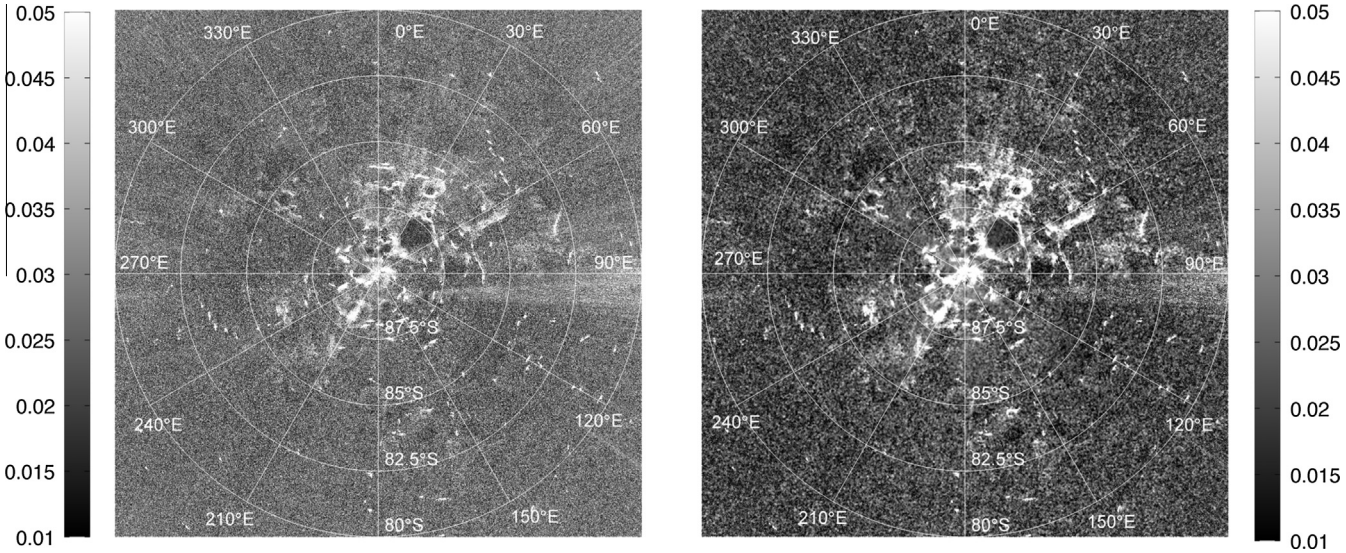

Fig. 1. LAMP off-band albedo, before (left) and after (right) processing as described in the text.

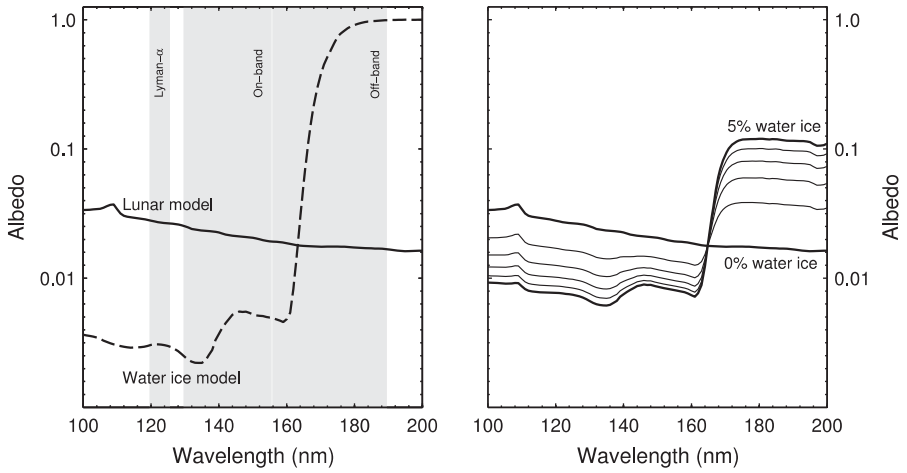

Fig. 2. Left: Modeled spectra of average lunar regolith (Hendrix et al., 2012) and water frost in the UV spectral region. The albedo values are directional-hemispheric reflectance, calculated using the two-stream radiative transfer model of Wiscombe and Warren (1980). Right: Modeled spectra for intimate mixtures of water ice in lunar regolith.

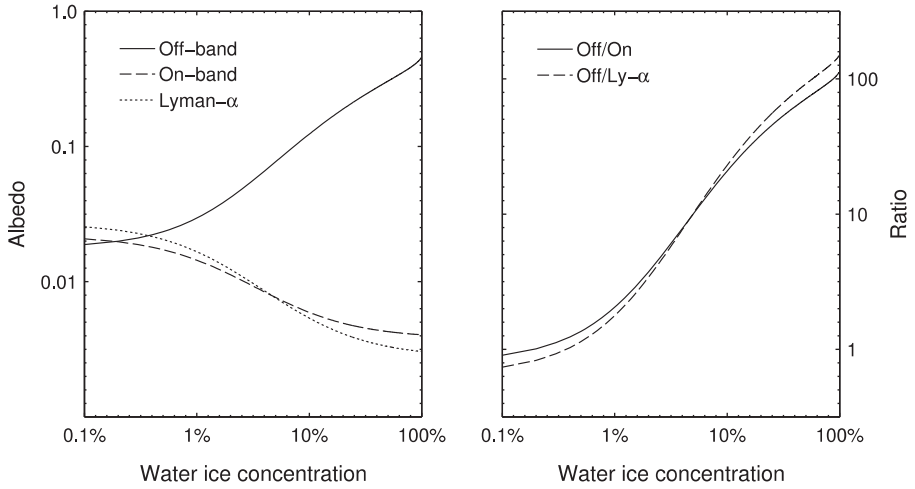

Fig. 3. Modeled variation in LAMP "off-band", "on-band", and Lyman-α albedo values for different water ice concentrations.

increasing water ice content, whereas on-band and Ly-α albedos decrease slowly. This behavior is shown in Fig. 3.

4. Results

4.1. UV albedo of lunar south polar cold traps

In illuminated regions where temperatures are far too warm for ice, the lunar off-band albedo is lower than both the on-band albedo and Lyman-α albedo, meaning that the spectrum of dry regolith has a "blue" slope in the UV. The mean off-band/on-band ratio of ~0.8 in these regions is consistent with the spectral model we derived from lunar-like optical constants above. Within the cold traps, as well as other anomalous regions, the spectral slope is reversed, becoming "red" in the wavelength range 100–200 nm. Although this is consistent with the UV spectrum of water ice, some of the features present in the south polar maps (Fig. 4) appear to be artifacts. In particular, the off-band and ratio maps show high values along crater rims and other features where temperatures are likely too high for stable ice. This may be due to inaccurate modeling of sky visibility and/or bidirectional reflectance on extreme slopes in the process of deriving albedo from LAMP's measured intensities (Gladstone et al., 2012). Nonetheless, areas of high off-band albedo are apparent even in the raw brightness maps, which seem to be correlated with specific craters and other surface features. As noted by Gladstone et al. (2012), the Lyman-α albedos of the permanently shadowed regions are clearly lower than in the illuminated terrain. We find that the on-band and Lyman-α albedos are moderately well correlated ($R = 0.21$), especially within the PSRs ($R = 0.32$). There is also a general pole-ward increase in the off-band/on-band albedo ratio, which appears independent of the larger PSRs (Fig. 5). A majority of the interior of Shackleton crater (89.6°S, 122°E), part of which has been suggested to harbor surface water ice deposits (Zuber et al., 2012; Thomson et al., 2012; Miller et al., 2014), is spectrally anomalous, having very high albedo in all three wavelength bands (Fig. 4). This spectral behavior is not consistent with the presence of exposed water ice (see spectra in Fig. 2), because the on-band albedo would be below the dry regolith value of ~0.03, when it is actually ~0.04 over much of Shackleton's interior. Spectra of at least some feldspars have both high on-band albedo and a high off/on-band albedo ratio, compared to pyroxenes (Wagner et al., 1987). However, we cannot rule out the case that Shackleton crater has an unusually feldspathic composition (e.g., pure anorthosite;

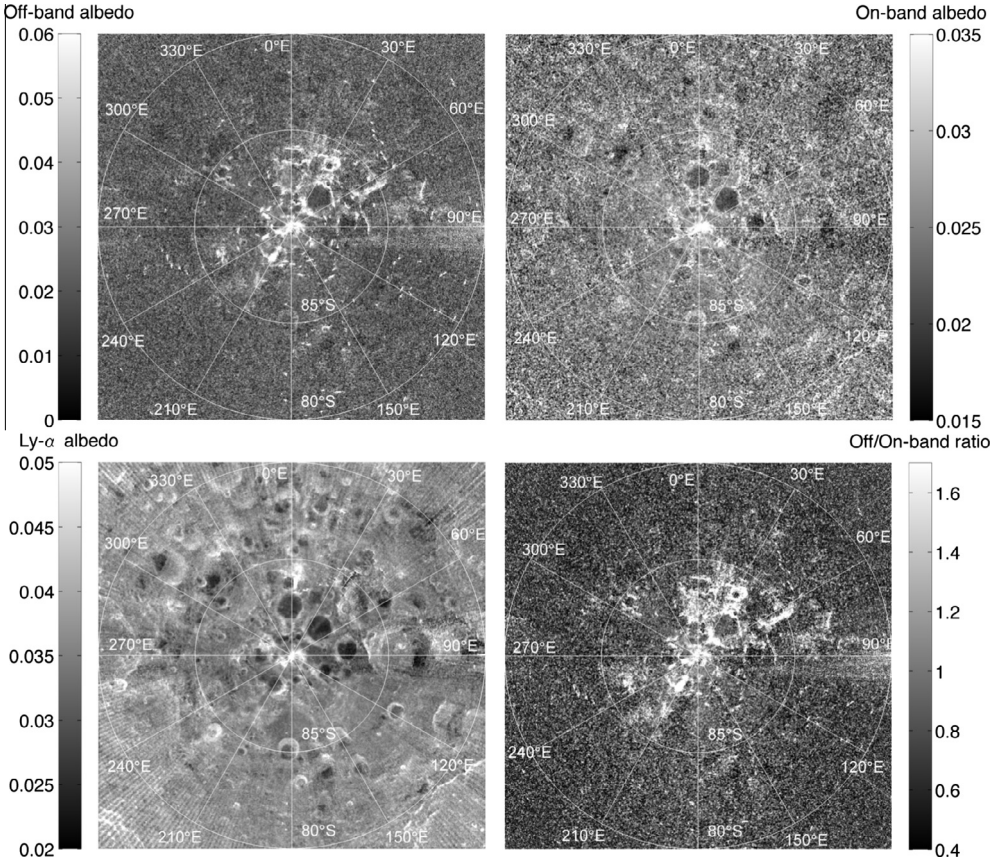

Fig. 4. LAMP ultraviolet albedo maps of the south polar region of the Moon. Apparent in the Lyman-α map are three large PSR craters near 0–90°E and 87–88°S: (clockwise from 0°E) Haworth, Shoemaker, and Faustini. Shackleton crater is located just off the pole at 120°E.

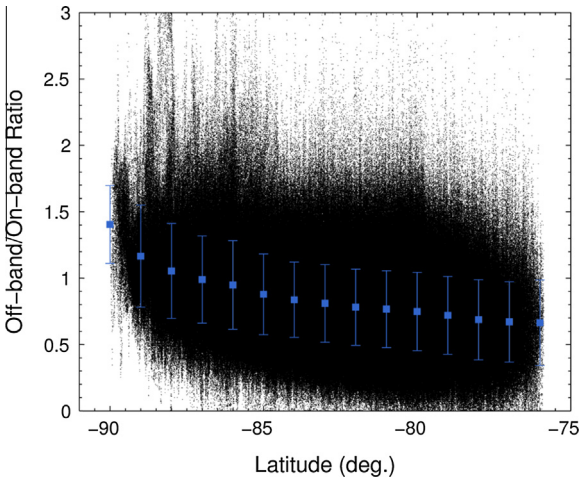

Fig. 5. Latitude dependence of LAMP off-band/on-band albedo ratio. A general monotonic pole-ward increase is observed in the data, including both illuminated and permanently shadowed terrain. Square symbols with error bars indicate the mean and standard deviation within each latitude bin.

Haruyama et al. (2013)) that displays a high albedo over all UV wavelengths, even when mixed with water ice.

4.2. Temperatures of lunar south polar cold traps

Diviner measurements show that the Moon's polar cold traps form a temperature population distinct from the illuminated terrain, based on both annual maximum (T_{max}) and annual average (T_{avg}) temperatures (Fig. 6). This is expressed as a bimodal distribution, with peaks near 230 K and 100 K in annual maximum temperature, and peaks near 120 K and 70 K for annual average temperature (Fig. 7). Defining a water ice cold trap as any location with T_{max} < 110 K (Watson et al., 1961; Vasavada et al., 1999), we find that the lunar south polar region (>82.5°S) contains $\sim 1.1 \times 10^4$ km^2 of cold trap area. We also note a rich diversity of thermal environments within and among the cold traps. In particular, we were interested in the three similarly sized (~50 km diameter) craters near the lunar south pole: Haworth, Shoemaker, and Faustini (Fig. 8). Previous studies using epithermal neutron emissions have provided evidence for concentrations of hydrogen-bearing species (presumably water) within these three craters, with varying abundances among them. Boynton et al. (2012) found that among the three craters, Shoemaker has the highest H abundance, followed by Faustini. Haworth shows some H-enhancement near its northwestern rim, but is otherwise similar to the background levels. It is important to note that the epithermal neutron counts measured from orbit by both the LRO and Lunar Prospector neutron instruments are sensitive to H concentrations within the top ~1 m, whereas the LAMP data used in this study probe the very surface, ~0.1–1 μm.

Diviner data indicate that among these three craters, Haworth is the coldest, with $T_{max} \sim 60$–80 K (full-width at half maximum), followed by Shoemaker with $T_{max} \sim 70$–95 K, and Faustini with $T_{max} \sim 85$–95 K (Fig. 9). The three craters show a similar pattern in mean annual temperature. This result was not obvious from models (Paige et al., 2010a) and indicates that subtle differences in incident radiative fluxes due to local topography and possibly unusual thermophysical properties (e.g. due to porosity or ice content) may drive relative differences at these cryogenic temperatures.

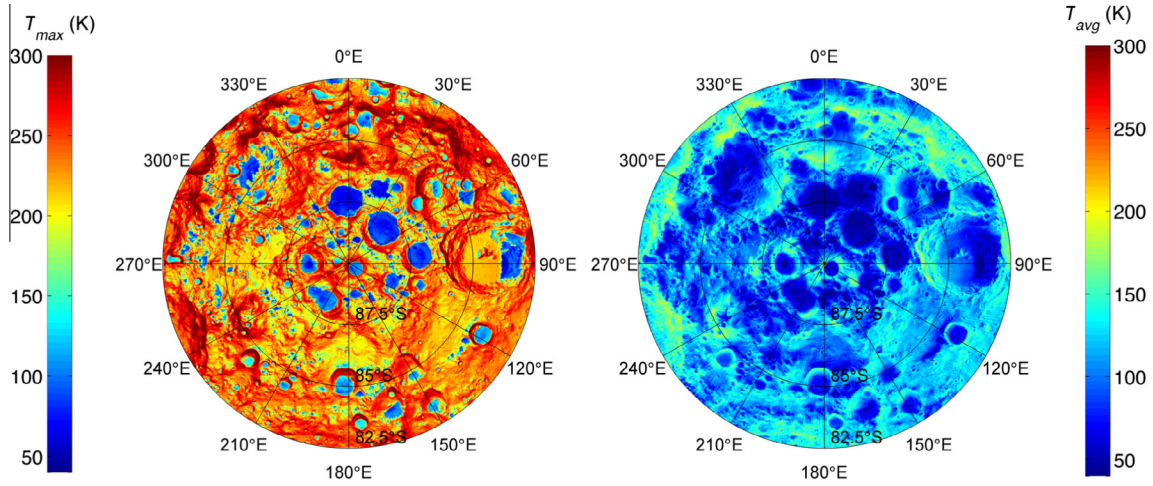

Fig. 6. Annual maximum (left) and annual average (right) bolometric surface temperatures as measured by Diviner, for the lunar south polar region >82.5°S.

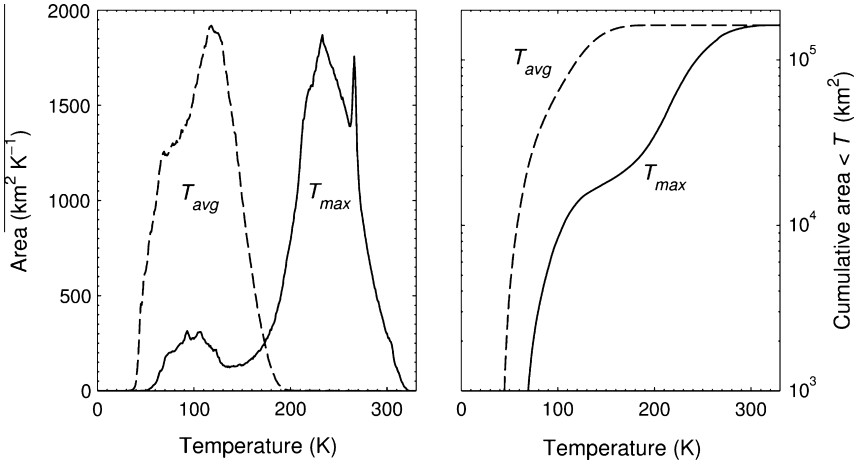

Fig. 7. Histograms of the Moon's south polar annual maximum and annual average temperatures, for latitudes >82.5°S.

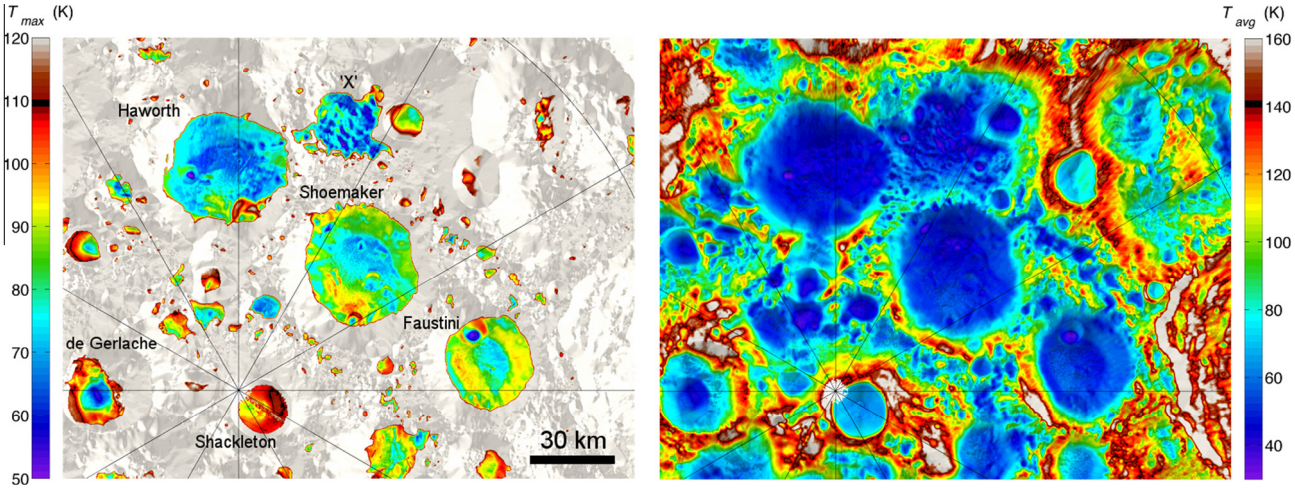

Fig. 8. Annual maximum (left) and annual average temperatures in the region of interest near the lunar south pole, containing three similarly sized craters: Haworth, Shoemaker, and Faustini. The black bar on the color scales indicate the chosen thermal stability criteria for surface water frost (T_{max} < 110 K) and subsurface water ice (T_{avg} < 140 K) (Schorghofer, 2008). The cold trap labeled 'X' is an especially cold, relatively flat PSR within a highly degraded unnamed crater.

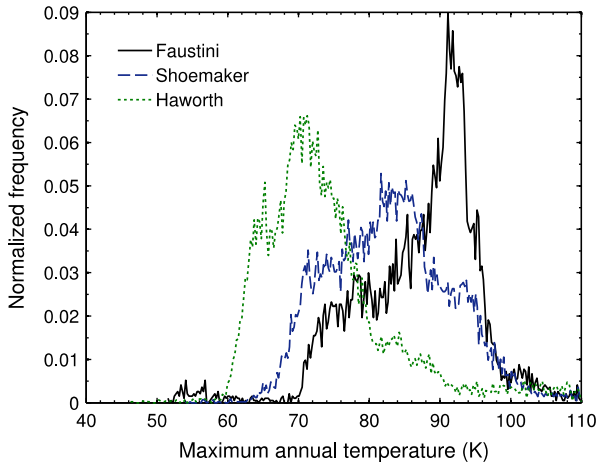

Fig. 9. Histograms of annual maximum temperature for three craters of interest: Faustini, Shoemaker, and Haworth. Note that Haworth is significantly colder than the other two craters, although all three have a significant area with $T_{max} < 90$ K.

Although they may appear minor, temperature differences of ~10 K in annual maximum temperature may cause significant differences in volatile accumulation rates and retention. When exposed to vacuum, the sublimation rate (kg m^{-2} s^{-1}) of a substance with molecular mass μ and equilibrium vapor pressure p_v at temperature T is given by (Estermann, 1955):

$$\dot{E}_{sub} = p_v(T)\sqrt{\mu/2\pi RT}, \quad (2)$$

where R is the universal gas constant. With appropriate constants for water (CRC Handbook, 2003), the sublimation rate at 70 K is ~10^{-5} times smaller than the sublimation rate at 80 K, and ~10^{-9} times smaller than at 90 K. Whether or not this can lead to measurable differences in water frost cover depends on the rates of supply and destruction of H_2O molecules, and their residence times within the various cold traps (Watson et al., 1961; Arnold, 1979). We write the surface mass balance as

$$\frac{dm}{dt} = \dot{S} - \dot{E}_{sub} - \dot{E}_* - \dot{E}_g, \quad (3)$$

where $\dot{S}$ is the supply rate (accounting for all sources), $\dot{E}_*$ is the loss rate due to photodissociation and sputtering, and $\dot{E}_g$ is the loss rate due to impact gardening. We can define a timescale associated with losing or gaining a mass of H_2O via each process; for example $t_* \sim m/\dot{E}_*$ is the timescale for destroying a mass m of ice by photodissociation and sputtering by the solar wind. The residence time for a layer of ice with thickness d subject only to sublimation is $t_{sub} \sim \rho d/\dot{E}_{sub}$, where ρ (≈970 kg m^{-3}) is the density of ice. As an illustration of the extremely nonlinear dependence of sublimation rate on temperature, the residence time of a monolayer at 100 K is 600 years, while at 70 K its residence time is over one hundred trillion years. Because of this steep decline in sublimation rate with decreasing temperature, there should be a characteristic temperature T_0, at which $\dot{E}_{sub} = \dot{S} - \dot{E}_* - \dot{E}_g$, such that no net mass gain or loss occurs (i.e. equilibrium). The exception is the case where $\dot{S} < \dot{E}_* + \dot{E}_g$, and no accumulation of ice is possible at any temperature. A positive detection of surface frost anywhere on the Moon would then be confirmation that this inequality is not satisfied, meaning that supply rates at least locally outcompete non-thermal losses. Next, if surface frost were found only below a specific temperature T_0, this would place a constraint on the quantity $(\dot{S} - \dot{E}_* - \dot{E}_g) \sim E_{sub}(T_0)$, such that the supply rate minus the non-thermal losses is comparable to the sublimation rate.

Impact gardening serves to mix surface frosts with regolith, leading to local homogeneity in ice concentration within the upper ~1 mm on timescales of ~10 Myr (Hurley et al., 2012). This allows us to place a theoretical constraint on the rate of effective surface ice mass loss as it is distributed to depth z: $\dot{E}_g \sim \rho(z/t_g)$. Using the $z/t_g \sim 0.1$ mm Myr^{-1} gardening rate based on the Hurley et al. (2012) model yields $\dot{E}_g \sim 10^{-15}$ kg m^{-2} s^{-1}, or ~10^{11} H_2O molecules per meter squared per second. This rate is comparable to the sublimation rate at ~110 K, meaning that on ~10 Myr timescales, impact gardening is important (relative to sublimation) as a loss process for surface ice, at all temperatures low enough to cold trap ice. In other words, a thin layer of ice (e.g. ~0.1–1 μm) will be lost by downward mechanical diffusion due to impact gardening on a timescale equal to or faster than sublimation loss. In reality, the Hurley et al. (2012) model showed that ice concentration is likely to be heterogeneous on a range of scales, and loss due to gardening is a complex process depending on initial conditions and the stochastic impact excavation process. Nonetheless, the calculation above shows that impact gardening could be an important loss process for surface frosts.

4.3. Correlations between temperature and UV albedo

Temperature is the fundamental quantity controlling sublimation rates of water frost, which is thermodynamically stable on billion-year timescales below temperatures of ~110 K (Vasavada et al., 1999). In addition to water, many other volatile species delivered by comets or outgassing from the lunar interior may be cold trapped at the Moon's poles (Zhang and Paige, 2009; Colaprete et al., 2010). If water ice is exposed at the surface, it might preferentially accumulate on the coldest surfaces, or alternatively, might be more prevalent at moderate temperatures, where vertical migration of water molecules from the subsurface is more efficient (Siegler et al., 2011; Schorghofer and Aharonson, 2014). We analyzed the annual maximum bolometric temperature from Diviner together with each of the three LAMP wavelength bands (Fig. 10). Several features are immediately obvious: (1) for temperatures >~110 K, off-band and on-band albedos show little correlation with temperature; (2) Lyman-α albedo shows a negative correlation with temperature beginning near ~110 K and continuing down to ~65 K; (3) off-band/on-band albedo ratios show the highest values at temperatures <110 K, with a peak near ~65 K. However, we caution that the downward trend in the ratio at temperatures <65 K may be an artifact due to the small number of points below this temperature. Finally, we note that above 200 K, the Lyman-α and on-band albedos show a positive trend with increasing temperature. Although this trend in absorption is probably not related to water frost, it may be a signal of the abundance of hydrogen in the form of adsorbed water or hydroxyl (McCord et al., 2011). Desorption of H_2O from regolith grain surfaces occurs over a range of temperatures, with lifetimes of several lunar days even above 200 K (Hibbitts et al., 2011; Poston et al., 2013). Therefore, it is possible (or indeed likely) that increasing concentrations of adsorbed H_2O/OH molecules with decreasing temperature in the range 200–300 K could produce the observed behavior.

Some locations have high off-band/on-band ratios, but also high on-band albedos, as noted for Shackleton crater above. For the purposes of this analysis, we assumed that these properties were due to anomalous silicate compositions (e.g. pure anorthosite, Haruyama et al., 2013) or space weathering effects (Hendrix and Vilas, 2006), because they are not consistent with enhanced water ice. Many more points display spectra fully consistent with surface exposures of water ice: high off-band albedo, low on-band and Lyman-α albedo, and high off-band/on-band albedo ratio.

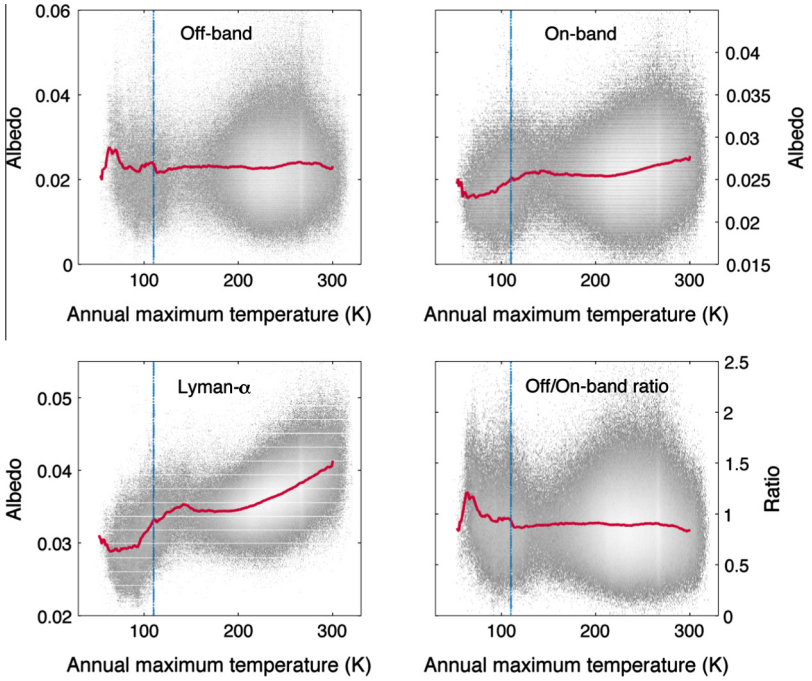

Fig. 10. Scatter plots of LAMP ultraviolet albedo data and Diviner annual maximum temperature data, with shades of gray indicating the local density of points. Note the spike in off-band/on-band albedo at temperatures <110 K (vertical dashed line), consistent with the sublimation temperature of H_2O. The solid lines show the mean of the data points within each 1° temperature bin.

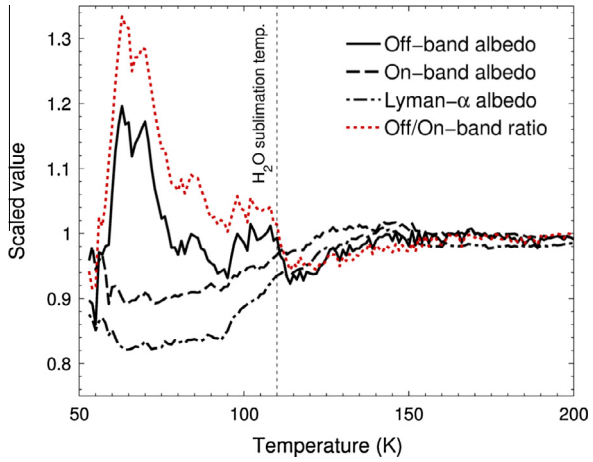

Fig. 11. LAMP albedo compared to Diviner annual maximum temperatures. The data are binned in 1 K increments, and scaled to the mean values from 110 to 300 K. Note the large increase in water ice-like features at temperatures <110 K: high off-band/on-band ratio, low on-band and Ly-α albedo.

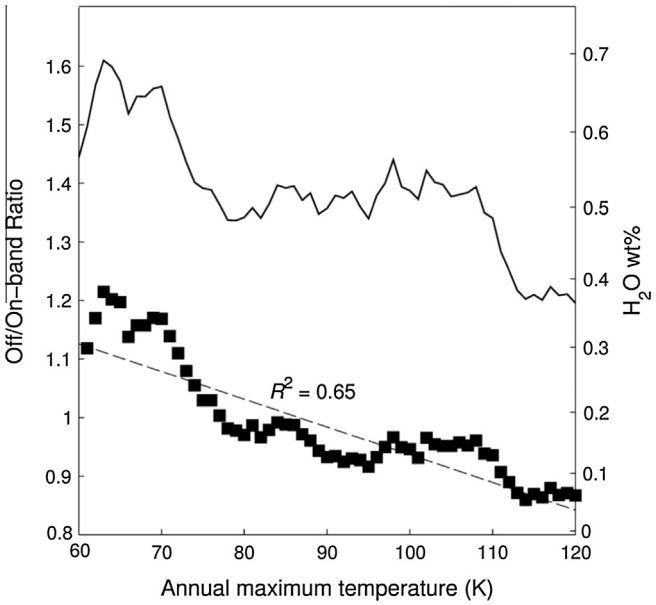

Fig. 12. Off/on-band albedo ratio for points within the cold traps, 60 K < T_{max} < 120 K. The filled squares show the mean value for each temperature bin, and the solid line shows one standard deviation from the mean. The right axis shows the modeled H_2O ice mixing ratio.

Furthermore, these points are strongly correlated with temperatures in ~60–110 K range, where ice is thermodynamically stable. Figs. 11 and 12 illustrate the sudden change in spectral properties at ~110 K. Note that there appear to be two peaks in the off-band albedo data: the first near 110 K, and the second near 65 K. However, the first peak is less apparent in the off-band/on-band ratio data. If real, we propose two different hypotheses to explain these peaks: (1) there are two populations of water ice deposits, with older deposits tending towards locations near ~110 K, and younger deposits preferring the coldest temperatures; (2) the first peak is due to water ice, and the second is due to carbon dioxide ice. We briefly explore each of these hypotheses below.

At the low end of the temperature range, water ice is so thermodynamically stable that it may be susceptible to non-thermal destruction and loss processes. For example, impact gardening may re-distribute water ice from the surface to subsurface. Above, we estimated that this transition occurs at ~110 K, which is very near the gap between the two hypothetical ice populations. The proposed mechanism for separating these two ice populations is that although water molecules are preferentially cold-trapped by the coldest surfaces, over time these ultra-cold ice deposits are redistributed or buried by impact gardening, because the water molecules are too immobile to migrate back

to the surface. However, water molecules on surfaces near 110 K are mobile enough to migrate back to the surface after being buried. This is possible, because the lunar heat flow of ~20 mW m^{-2} (Langseth et al., 1976) creates temperature gradients of ~1–3 K m^{-1}, increasing downwards. Therefore, any ice that was previously driven downward by impact gardening would continuously resupply the surface. This hypothesis could be tested by determining the subsurface ice content at both very cold ($T_{max} \ll 110$ K) and moderately cold ($T_{max} \sim 110$ K) sites; the ice should be more homogeneously distributed with depth at the colder sites. Isotope ratios might also help determine the relative ages of surface ice, based on the assumption that older ice would be depleted in lighter isotopes due to the mass-dependent fractionation caused by gradual sublimation.

Our second hypothesis is that both H_2O and CO_2 ices are present on the Moon. A major component of comets (~10% relative to H_2O; Bockelée-Morvan et al. (2011)), CO_2 is also one of the most ubiquitous volatile species on terrestrial planet surfaces and within their atmospheres. Its presence within sufficiently cold lunar cold traps would therefore not be surprising. Zhang and Paige (2009) estimated the effective sublimation temperatures for a large collection of volatiles, and found CO_2 to be thermodynamically stable at $T_{max} <$ ~60 K (losing ~1 m Gyr^{-1} at this temperature). Although the second peak in Fig. 11 occurs near ~65 K, this is only marginally above the estimated sublimation temperature of CO_2, which may simply reflect enhanced stability due to bonding with mineral grains, for example. In this case, the same principle applied above to maintaining surface water ice deposits near ~110 K would apply to maintaining surface carbon dioxide ice deposits near ~65 K. A model UV reflectance spectrum based on laboratory measurements of CO_2 ice optical constants (Hansen, 2005) shows high albedo in the off-band wavelengths, but also higher albedo in the Lyman-α band (Fig. 13). For this model, the optical constants have been interpolated across a gap from 130 to 174 nm (G.B. Hansen, personal communication). Although the blue slope from 120 to 140 nm is inconsistent with typical LAMP measurements of the PSRs, differences in particle size and geometry can significantly affect the reflectance of solid CO_2 in this region (Hapke, 1981; Hendrix et al., 2010). The results for CO_2 are therefore inconclusive, and a better match is still found for H_2O. Other volatiles having sublimation temperatures near 65 K include ammonia (NH_3) and sulfur dioxide (SO_2), but these compounds are both relatively dark in LAMP's on-band spectral region.

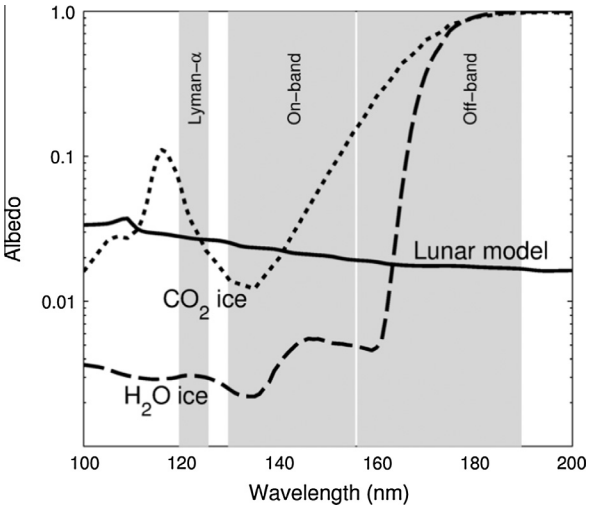

Fig. 13. CO_2 ice spectrum compared to lunar regolith and water ice. The albedo shown is the directional–hemispherical reflectance, calculated using the model of Wiscombe and Warren (1980).

An alternative hypothesis for the low UV albedo of the Moon's polar cold traps is enhanced porosity, rather than water ice (Gladstone et al., 2012). Examining the relative spectral variations, as shown in Fig. 10, we can test this hypothesis. The effect of increasing porosity is to darken the surface at all wavelengths (Hapke, 2008). While this would be consistent with the darkening observed in the Lyman-α band and the on-band wavelengths, it is only consistent with the brightening in the off-band wavelengths at low temperatures if indeed water frost is present there and contributing to a spectral reddening effect that compensates for an otherwise low albedo. Therefore, the combined LAMP and Diviner observations show that high porosity is not the sole cause of the cold traps' anomalous spectra. While Gladstone et al. (2012) invoked the effects of porosity to avoid the implausible situation of copious ~10% or higher water frost abundances using their linear areal mixing assumption, as we discuss next, the use of the more realistic intimate mixing model and no porosity broadly results in abundances less than the ~5% value determined for Cabeus crater by the LCROSS mission (Colaprete et al., 2010).

4.4. Abundance of water ice

Based on the results presented in the preceding sections, the most plausible explanation for the anomalous UV reflectance of the Moon's south polar cold traps is the presence of exposed water ice (and possibly other volatiles). Using the albedo model results shown above, we can estimate the abundance of water ice within these regions. As shown in Fig. 10, the average off-band/on-band ratio for temperatures <110 K is ~1.0, with many locations having values >2. The peak in Fig. 11 shows that points having a temperature ~65 K have ~30% higher off-band/on-band ratios than illuminated terrain. The crater Sverdrup (88.5°S, 208°E) has the highest ratio values, ~3.0–4.0. From the model in Fig. 3, these values correspond to a range in water ice content of ~0.1% (ratio = 1.0) up to ~2% (ratio = 4.0). These calculations assume the ice is intimately mixed with the lunar regolith; if we instead assume the ice is patchy but pure, we find a range in ice area fraction of ~1% (ratio = 1.0) to ~10% (ratio = 4.0). The lower end of this range is consistent with the findings of Gladstone et al. (2012) for the average of the PSRs, based on a similar linear mixing model. Hydrogen abundances estimated from epithermal neutron counts are in general agreement with our estimates, corresponding to an average of ~1.5% H_2O by mass within the PSRs (Feldman et al., 2001). However, it should be noted that this hydrogen could be distributed anywhere within the upper ~1 m to appear in the neutron data, and not necessarily as a surface frost detectable by LAMP.

4.5. Distribution and origins of water ice

Our results indicate a highly heterogeneous spatial distribution of water frost on the lunar surface, even among those regions where water frost is thermally stable (Fig. 14). Although some of the coldest regions show UV albedos consistent with relatively high concentrations of water frost, several prominent cold-trap craters do not show evidence for water ice concentrations >0.1%. This may be analogous to the findings of Spudis et al. (2013) and Neish et al. (2011), which showed small craters within PSRs having circular polarization ratios consistent with water ice. Nonetheless, the general trend of increasing off-band/on-band albedo (higher H_2O abundance) with decreasing annual maximum temperature holds among the major south polar cold traps studied (Fig. 15; also see Appendix A). Importantly, the distribution of peak temperatures for locations with UV spectra consistent with exposed water frost (off/on-band ratio >1.2 and Ly-α albedo <0.03) is considerably

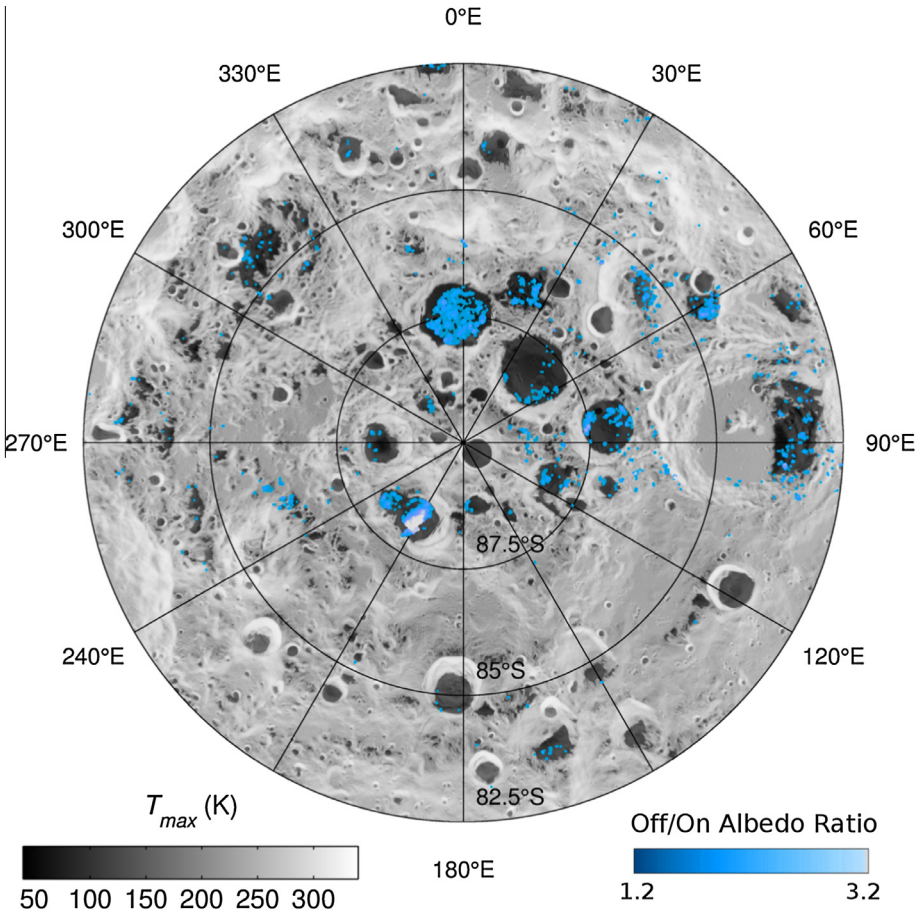

Fig. 14. Locations of anomalous UV albedo consistent with water ice. Colors indicate points with off/on-band albedo ratio values >1.2 and Lyman-α albedo <0.03, increasing from deep orange (1.2) to white (>3.2). The average Moon outside of the cold traps has a ratio of ~0.9. Ratio values in the range 1.2–4.0 are consistent with water ice concentrations of ~0.1–2.0% by mass. If patchy exposures of pure water ice are mixed by area with dry regolith, the abundance could be up to ~10%.

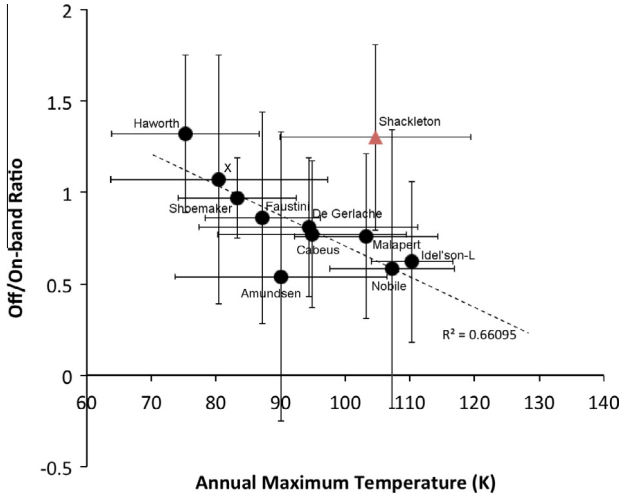

Fig. 15. LAMP off-band/on-band albedo ratios (higher indicates greater H_2O abundance) compared to Diviner annual maximum temperatures, for specific regions of interest, some of which are labeled in Fig. 5. The error bars correspond to one standard deviation in each parameter. Shackleton crater has an anomalous spectrum, which is generally inconsistent with exposed water frost; it is therefore excluded from the linear fit.

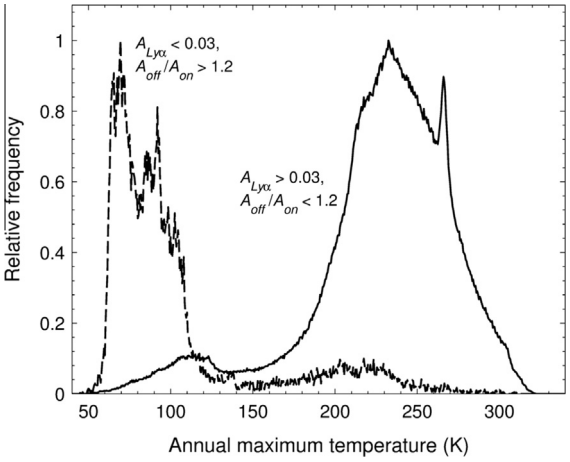

Fig. 16. Temperature histograms of points meeting the UV spectral criteria for exposed water frost, and the complementary set not meeting the criteria. For those locations meeting the UV criteria (Ly-α albedo <0.03 and off/on-band ratio >1.2), the vast majority has annual maximum temperature <110 K.

lower than the rest of the south polar region (Fig. 16). A comparative study of the three similar craters Haworth, Shoemaker, and Faustini yields valuable insight into the possible causes of the observed heterogeneity. Gladstone et al. (2012) noted that Shoemaker appears to harbor less water frost than the other two craters, and suggested that this implies that water delivery and loss rates are very similar. Using the analysis of Section 4.1 above

combined with the Diviner and LAMP data, we can quantitatively constrain these rates. The detection of water ice at the lunar surface is consistent with a scenario in which the supply rates are high enough to offset destruction rates at locations below a temperature T_0. Based on the observed changes in albedo as correlated with temperature, we find that $T_0 \approx 110$ K. This implies that the net supply rate (supply minus non-thermal losses), $(\dot{S} - \dot{E}_* - \dot{E}_g)$, is comparable to the sublimation rate at 110 K, $\dot{E}_{sub}(T_0) \sim 10^{-15}$ kg m^{-2} s^{-1}. We already estimated $\dot{E}_g \sim 10^{-15}$ kg m^{-2} s^{-1} on timescales of ~10 Myr, which itself is comparable to this limiting sublimation rate. While the results of Morgan and Shemansky (1991) suggested the loss rate due to photo-destruction and sputtering, $\dot{E}_*$, is larger than the source term, $\dot{S}$, Gladstone et al. (2012) estimated that these losses are actually comparable to their estimated source rate of $\sim 10^{-16}$ kg m^{-2} s^{-1}. At peak temperatures of ~110 K, the water ice sublimation rate is then at least an order of magnitude faster than photolysis and sputtering, implying the dominance of sublimation and impact gardening in removing surface ice. A balance between sublimation and gardening as loss and redistribution processes could explain the heterogeneous distribution of surface frosts within the cold traps, owing to their complex temperature distributions.

An important observation from comparison of the Diviner and LAMP data is that the peak in apparent water ice concentration occurs near ~65 K, with perhaps a smaller peak near 110 K (Fig. 11). Shoemaker crater, whose surface appears nearly devoid of significant quantities of water frost, has $T_{max} \sim 70$–95 K, in contrast to Haworth, which is observed to harbor significant ice with $T_{max} \sim 60$–80 K. On average, Faustini has lower apparent surface ice content, yet the coldest parts (<90 K) on its western side have higher apparent ice concentrations. If sublimation were the dominant process, it would be expected that ice concentrations would plateau for $T_{max} < 110$ K, which is not the case. We propose that the observed behavior is due to spatial mixing of variable temperatures and ice content within the instrument fields of view, as well as heterogeneity in the destruction processes, particularly impact gardening and space weathering (Hurley et al., 2012).

The subtle second peak in apparent ice concentration just below 110 K is intriguing (Fig. 11), and may indicate the existence of two populations of frosted surfaces: (1) those surfaces near the H_2O sublimation temperature, and (2) those surfaces cold enough that sublimation is entirely negligible. Ice driven downwards by impact gardening at sites in population (1) could be subsequently driven to the surface by sublimation and upward diffusion, due to the positive downward thermal gradient. This would not be possible within population (2) sites, where sublimation temperatures remain negligible relative to impact gardening rates at depths of up to several meters. Therefore, ice content should decrease downward at population (1) sites, and should be more or less homogeneously mixed within the gardening layer at population (2) sites, unless the H_2O source rate is much higher than the impact gardening rate of $\sim 10^{-15}$ kg m^{-2} s^{-1}.

5. Conclusions

Observational evidence from Diviner surface temperature measurements and LAMP ultraviolet albedo spectra is consistent with the presence of exposed water frost near the lunar south pole, with a distribution controlled by temperature. For locations with annual maximum temperatures $T_{max} < \sim 110$ K, we find a strong correlation between decreasing annual maximum temperature and: (a) decreasing Lyman-α albedo, (b) decreasing "on-band" (129.57–155.57 nm) albedo, and (c) increasing "off-band" (155.57–189.57 nm) albedo. All of these features are consistent with the UV spectrum of water ice, and are expected for water ice layers >~100 nm in thickness. High regolith porosity, which would darken the surface at all wavelengths, cannot alone explain the observed spectral variations with temperature. Given the observed LAMP off-band/on-band albedo ratios at a spatial scale of 250 m, the range of water ice concentrations within the cold traps with $T_{max} < 110$ K is ~0.1–2.0% by mass, if the ice is intimately mixed with dry regolith. If pure water ice is exposed instead, then up to ~10% of the surface area in some 250-m regions may be ice-covered. Note that these abundance estimates assume a two-component mixture, and could be in error if other volatiles or minerals are present in addition to water ice and highlands regolith.

The inferred distribution of exposed water ice is highly heterogeneous, with some cold traps <110 K having little to no apparent water frost, and others with a significant amount of water frost. As noted by Gladstone et al. (2012), this heterogeneity may be a consequence of the fact that the net supply rate of H_2O molecules to the lunar poles favors their net destruction only marginally, leaving open the possibility of many regions with differing susceptibilities to losses and sources. Because the sublimation rate of exposed water ice at 110 K of 10^{-15} kg m^{-2} s^{-1} is an order of magnitude larger than the rate of destruction by UV photolysis by Lyman-α from the interplanetary medium (Gladstone et al., 2012), the survival of water ice in a given location could depend sensitively on supply rates and peak temperature. The observed increase in ice abundance with decreasing temperature from ~110 K to 65 K suggests that sublimation is indeed the dominant loss process, and the rate of desorption of OH by UV photolysis were overestimated by Morgan and Shemansky (1991) Impact gardening becomes the dominant H_2O loss process where $T_{max} < 110$ K, and causes vertical and horizontal homogenization of ice content. For locations with $T_{max} < 110$ K, ice mixed downward by impact gardening may be resupplied to the surface, due to local thermal gradients. This is one possible explanation for the two observed populations of ice deposits, one peaking at $T_{max} \sim 100$ K, and the other peaking at $T_{max} \sim 65$ K: the first would correspond to older, warmer deposits where surface ice is resistant to downward diffusion, and the second would correspond to relatively younger surface frosts that have not yet been buried by impact gardening. Given the appropriate temperature cycles, diurnal or seasonal variations in surface frost are possible. Finally, we cannot rule out the possibility that the colder population of ice deposits may be due to other volatiles such as dioxide ice, although peak temperatures of ~65 K are slightly higher than the usual CO_2 sublimation temperature of ~60 K. The spectral appearance of mixtures of volatiles such as CO_2 and regolith should be investigated as a next step. Future remote sensing measurements could address these ambiguities by looking for vibrational absorption features specific to each candidate molecule, provided some means of sensing in the dark.

Acknowledgments

We thank Brad Thomson and an anonymous reviewer for their constructive criticism, which greatly improved this paper. Part of this work was performed at the Jet Propulsion Laboratory, California Institute of Technology, under contract with the National Aeronautics and Space Administration.

Appendix A

Temperatures and ultraviolet albedos of important south polar PSRs

PSR	$\langle T_{max} \rangle$	$\sigma(T_{max})$	⟨Off/on⟩	σ(Off/on)	⟨Lyman-α⟩	σ(Ly-α)	⟨On⟩	σ(On)	⟨Off⟩	σ(Off)
Amundsen	90.05	16.38	0.54	0.79	0.03	0.004	0.023	0.0044	0.02	0.0087
Cabeus	94.84	14.6	0.77	0.4	0.03	0.0036	0.022	0.0032	0.0183	0.0062
De Gerlache	94.3	16.9	0.81	0.38	0.03	0.003	0.024	0.0027	0.021	0.0078
Faustini	87.21	8.93	0.86	0.58	0.027	0.0038	0.023	0.004	0.022	0.012
Haworth	75.28	11.4	1.32	0.43	0.03	0.0035	0.024	0.0033	0.033	0.0079
Malapert	103.2	11.1	0.76	0.45	0.033	0.0031	0.024	0.0036	0.02	0.0077
Memorial	80.47	16.8	1.07	0.68	0.032	0.0028	0.025	0.0031	0.03	0.011
Nobile	107.2	9.67	0.58	0.76	0.031	0.0037	0.023	0.0042	0.02	0.0084
Idel'son-L	110.3	6.33	0.62	0.44	0.033	0.0028	0.025	0.0037	0.017	0.0065
Shackleton	104.6	14.8	1.3	0.51	0.042	0.0058	0.033	0.005	0.046	0.012
Shoemaker	83.27	9.13	0.97	0.22	0.028	0.0033	0.023	0.0028	0.022	0.0056

References

Arnold, J.R., 1979. Ice in the lunar polar regions. J. Geophys. Res. 84 (B10), 5659–5668.

Bockelée-Morvan, D., 2011. An overview of comet composition. Proc. Int. Astron. Union 7 (S280), 261–274.

Boynton, W.V. et al., 2012. High spatial resolution studies of epithermal neutron emission from the lunar poles: Constraints on hydrogen mobility. J. Geophys. Res.: Planets (1991–2012) 117 (E12).

Campbell, D.B. et al., 2006. No evidence for thick deposits of ice at the lunar south pole. Nature 443 (7113), 835–837.

Colaprete, A. et al., 2010. Detection of water in the LCROSS ejecta plume. Science 330 (6003), 463–468.

CRC Handbook of Chemistry and Physics, 84th ed. Lide, D.R. (Ed.), 2003.

Estermann, I., 1955. Gases at low densities. In: Rossini, F.D. (Ed.), Thermodynamics and Physics of Matter, High Speed Aerodynamics and Jet Propulsion, vol. 2. Princeton University Press, Princeton, NJ, pp. 742–744.

Feldman, W.C. et al., 1998. Fluxes of fast and epithermal neutrons from Lunar Prospector: Evidence for water ice at the lunar poles. Science 281 (5382), 1496–1500.

Feldman, W.C. et al., 2001. Evidence for water ice near the lunar poles. J. Geophys. Res.: Planets 106 (E10), 23231–23251.

Gladstone, G.R. et al., 2010a. LRO-LAMP observations of the LCROSS impact plume. Science 330 (6003), 472–476.

Gladstone, G.R. et al., 2010b. LAMP: The Lyman Alpha Mapping Project on NASA's Lunar Reconnaissance Orbiter mission. Space Sci. Rev. 150 (1–4), 161–181.

Gladstone, G.R. et al., 2012. Far-ultraviolet reflectance properties of the Moon's permanently shadowed regions. J. Geophys. Res.: Planets 117 (E12).

Hansen, G.B., 2005. Ultraviolet to near-infrared absorption spectrum of carbon dioxide ice from 0.174 to 1.8 μm. J. Geophys. Res.: Planets (1991–2012) 110 (E11).

Hapke, B., 1981. Bidirectional reflectance spectroscopy: 1. Theory. J. Geophys. Res.: Solid Earth (1978–2012) 86 (B4), 3039–3054.

Hapke, B., 1993. Theory of Reflectance Spectroscopy. Cambridge University Press.

Hapke, B., 2008. Bidirectional reflectance spectroscopy: 6. Effects of porosity. Icarus 195 (2), 918–926.

Haruyama, J. et al., 2008. Lack of exposed ice inside lunar south pole Shackleton crater. Science 322 (5903), 938–939.

Haruyama, J. et al., 2013. An explanation of bright areas inside Shackleton crater at the lunar south pole other than water–ice deposits. Geophys. Res. Lett. 40 (15), 3814–3818.

Hayne, P.O. et al., 2010. Diviner lunar radiometer observations of the LCROSS impact. Science 330 (6003), 477–479.

Hendrix, A.R., Hansen, C.J., Holsclaw, G.M., 2010. The ultraviolet reflectance of Enceladus: Implications for surface composition. Icarus 206 (2), 608–617.

Hendrix, A.R., Vilas, F., 2006. The effects of space weathering at UV wavelengths: S-class asteroids. Astron. J. 132 (3), 1396.

Hendrix, A.R. et al., 2012. The lunar far-UV albedo: Indicator of hydration and weathering. J. Geophys. Res. 117 (E12).

Hibbitts, C.A. et al., 2011. Thermal stability of water and hydroxyl on the surface of the Moon from temperature-programmed desorption measurements of lunar analog materials. Icarus 213 (1), 64–72.

Hurley, D.M. et al., 2012. Two-dimensional distribution of volatiles in the lunar regolith from space weathering simulations. Geophys. Res. Lett. 39 (9), L09203.

Langseth, M.G., Keihm, S.J., Peters, K., 1976. Revised lunar heat-flow values. Proc. Lunar Sci. Conf. 7, 3143–3171.

Lucey, P.G. et al., 2014. The global albedo of the Moon at 1064-nm from the Lunar Orbiter Laser Altimeter (LOLA). J. Geophys. Res., 1665–1679

McCord, T.B. et al., 2011. Sources and physical processes responsible for OH/H_2O in the lunar soil as revealed by the Moon Mineralogy Mapper (M3). J. Geophys. Res.: Planets (1991–2012) 116 (E6).

Miller, R.S., Lawrence, D.J., Hurley, D.M., 2014. Identification of surface hydrogen enhancements within the Moon's Shackleton crater. Icarus 233, 229–232.

Morgan, T.H., Shemansky, D.E., 1991. Limits to the lunar atmosphere. J. Geophys. Res. 96 (A2), 1351–1367.

Neish, C.D. et al., 2011. The nature of lunar volatiles as revealed by Mini-RF observations of the LCROSS impact site. J. Geophys. Res.: Planets (1991–2012) 116 (E11).

Nozette, S. et al., 1996. The Clementine bistatic radar experiment. Science 274 (5292), 1495–1498.

Paige, D.A. et al., 2010a. Diviner lunar radiometer observations of cold traps in the Moon's south polar region. Science 330 (6003), 479–482.

Paige, D.A. et al., 2010b. The Lunar Reconnaissance Orbiter diviner lunar radiometer experiment. Space Sci. Rev. 150 (1–4), 125–160.

Poston, M.J. et al., 2013. Water interactions with micronized lunar surrogates JSC-1A and albite under ultra-high vacuum with application to lunar observations. J. Geophys. Res.: Planets 118 (1), 105–115.

Schorghofer, N., 2008. The lifetime of ice on main belt asteroids. Astrophys. J. 682 (1), 697.

Schorghofer, N., Aharonson, O., 2014. The lunar thermal ice pump. Astrophys. J. 788 (2), 169.

Schultz, P.H. et al., 2010. The LCROSS cratering experiment. Science 330 (6003), 468–472.

Sefton-Nash, E., Williams, J.-P., Paige, D.A., 2014. Modeling, gridding and storage of effective fields of view for terascale, point-based planetary datasets: Case study – LRO Diviner. Lunar Planet. Sci. 45. Abstract #2737.

Siegler, M.A., Bills, B.G., Paige, D.A., 2011. Effects of orbital evolution on lunar ice stability. J. Geophys. Res.: Planets (1991–2012) 116 (E3).

Slade, M.A., Butler, B.J., Muhleman, D.O., 1992. Mercury radar imaging: Evidence for polar ice. Science 258 (5082), 635–640.

Spudis, P.D. et al., 2013. Evidence for water ice on the Moon: Results for anomalous polar craters from the LRO Mini-RF imaging radar. J. Geophys. Res.: Planets 118 (10), 2016–2029.

Stacy, N.J.S., Campbell, D.B., Ford, P.G., 1997. Arecibo radar mapping of the lunar poles: A search for ice deposits. Science 276 (5318), 1527–1530.

Thomson, B.J. et al., 2012. An upper limit for ice in Shackleton crater as revealed by LRO Mini-RF orbital radar. Geophys. Res. Lett. 39 (14), L14201.

Vasavada, A.R., Paige, D.A., Wood, S.E., 1999. Near-surface temperatures on Mercury and the Moon and the stability of polar ice deposits. Icarus 141 (2), 179–193.

Wagner, J.K., Hapke, B.W., Wells, E.N., 1987. Atlas of reflectance spectra of terrestrial, lunar, and meteoritic powders and frosts from 92 to 1800 nm. Icarus 69 (1), 14–28.

Warren, S.G., Brandt, R.E., 2008. Optical constants of ice from the ultraviolet to the microwave: A revised compilation. J. Geophys. Res.: Atmos. (1984–2012) 113 (D14).

Watson, K., Murray, B.C., Brown, H., 1961. The behavior of volatiles on the lunar surface. J. Geophys. Res. 66 (9), 3033–3045.

Wiscombe, W.J., Warren, S.G., 1980. A model for the spectral albedo of snow. I: Pure snow. J. Atmos. Sci. 37 (12), 2712–2733.

Zhang, J.A., Paige, D.A., 2009. Cold-trapped organic compounds at the poles of the Moon and Mercury: Implications for origins. Geophys. Res. Lett. 36 (16), L16203.

Zuber, M.T. et al., 2012. Constraints on the volatile distribution within Shackleton crater at the lunar south pole. Nature 486 (7403), 378–381.